

Probing momentum-dependent scattering in uniaxially stressed Sr_2RuO_4 through the Hall effect

Po-Ya Yang,¹ Hilary M. L. Noad,¹ Mark E. Barber,^{1,2,3} Naoki Kikugawa,⁴
Dmitry Sokolov,¹ Andrew P. Mackenzie,^{1,5} and Clifford W. Hicks^{6,1}

¹Max Planck Institute for Chemical Physics of Solids, Nöthnitzer Str 40, 01187 Dresden, Germany

²Department of Applied Physics, Stanford University, Stanford, CA 94305, USA

³Geballe Laboratory for Advanced Materials, Stanford, CA 94305, USA

⁴National Institute for Materials Science, Tsukuba 305-0003, Japan

⁵Scottish Universities Physics Alliance, School of Physics and Astronomy,
University of St. Andrews, St. Andrews KY16 9SS, U.K.

⁶School of Physics and Astronomy, University of Birmingham, Birmingham B15 2TT, U.K.

(Dated: February 17, 2023)

Under in-plane uniaxial stress, the largest Fermi surface sheet of the correlated metal Sr_2RuO_4 undergoes a Lifshitz transition from an electron-like to an open geometry. We investigate the effects of this transition on transport through measurement of the longitudinal resistivity ρ_{xx} and the Hall coefficient R_H . At temperatures where scattering is dominated by electron-electron scattering, R_H becomes more negative across the Lifshitz transition, opposite to expectations from the change in Fermi surface topology. We show that this change in R_H is explainable only if scattering changes throughout the Brillouin zone, not just at the point in k -space where the Lifshitz transition occurs. In a model of orbital-dependent scattering, the electron-electron scattering rate on sections of Fermi surface with xy orbital weight decreases dramatically. On the other hand, at temperatures where defect scattering dominates ρ_{xx} and R_H are essentially constant across the Lifshitz transition.

Introduction. The Hall coefficient R_H of multi-band metals is a challenging quantity to analyze. In the low-field limit, it is determined by an integral of the mean free path around the Fermi surfaces [1]. It can therefore be used to probe the momentum dependence of scattering in metals with simple Fermi surfaces [2–4]. However, as complexity increases models become badly underconstrained. The case of the correlated metal and superconductor Sr_2RuO_4 [5] highlights the challenge. With 1% substitution of La onto the Sr site, the low-temperature Hall coefficient changes from electron-like to hole-like, even though the Fermi surfaces are almost unchanged [6, 7].

The advent of strain tuning might make R_H a more broadly useful measurement quantity. By correlating changes in R_H with specific strain-driven changes in electronic structure, models of scattering can be tested with greater rigor. Crucially, if the deformation is elastic the defect landscape is not altered.

Here, we study Sr_2RuO_4 , which has become an important test case for understanding of correlated electron materials [8–10]. It is a highly two-dimensional metal, in which correlations renormalize but do not destroy Landau quasiparticles [11, 12]. Under uniaxial stress σ applied along the [100] lattice direction, the largest Fermi surface sheet [the γ sheet— see Fig. 1(a)] undergoes a Lifshitz transition from an electron-like to an open geometry [13]. This transition is illustrated in Fig. 1(b). It has been reported to occur at $\sigma = \sigma_L = -0.71 \pm 0.08$ GPa [14], where negative values denote compression. Under the common assumption that the Hall effect is determined by the topology of the Fermi sur-

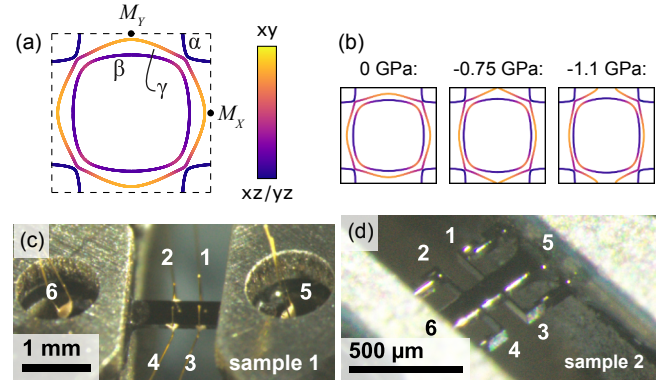


FIG. 1. (a) Model Fermi surfaces of Sr_2RuO_4 , coloured by orbital weight, from Ref. [17]. (b) Fermi surfaces calculated under uniaxial stresses along [100] of 0, -0.75 , and -1.1 GPa. (c,d) Photographs of samples 1 and 2.

faces, this transition should make R_H more positive. If scattering time rather than mean free path is isotropic, the quantitative change in R_H might be small, but is still expected to be positive [15, 16].

We report here that in fact the Lifshitz transition makes R_H more *negative*, opposite to the expectation from the change in Fermi surface topology. Furthermore, the magnitude of the change implies changes in scattering throughout the Brillouin zone: going through the Lifshitz transition appears to make Sr_2RuO_4 a considerably less-strongly correlated metal. Sr_2RuO_4 therefore provides an important example of how electronic correlations emerge in metals, and how correlations may potentially be “switched on and off.”

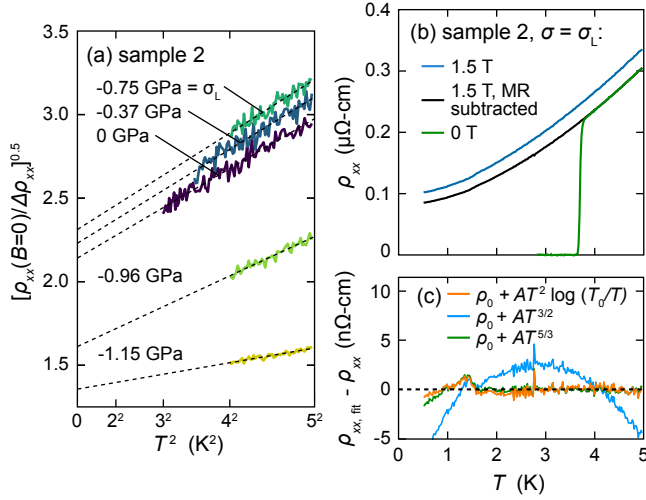


FIG. 2. (a) $[\rho_{xx}(B=0)/\Delta\rho_{xx}]^{0.5}$, where $\Delta\rho_{xx}$ is the change in ρ_{xx} between 0 and 1.5 T, against T^2 for sample 2 at various stresses. The dashed lines are linear fits. (b) $\rho_{xx}(T)$ of sample 2 at $\sigma = \sigma_L = -0.75$ GPa. The black line is an average of data at +1.5 and -1.5 T, with the magnetoresistance subtracted as described in the text. (c) The difference between various fitting models and the black line in panel (b).

Methods. Measurements were performed using a piezoelectric-driven uniaxial stress device similar to that described in Ref. [18], that incorporates sensors of both the applied displacement and applied force. As in Ref. [19], samples were mounted onto carriers, which were then mounted onto the cell. These carriers comprise two parts, and the sample is compressed when they are brought together. This mechanism allows in situ calibration of the zero-force reading of the force sensor.

Two samples, photographed in Figs. 1(c,d), were studied. Sample 1 is a beam of constant cross-section with electrical contacts attached by hand, while for sample 2 a plasma focused ion beam was used to mill contacts from the sample itself. The residual resistivities are 0.4 and $0.09 \mu\Omega\text{-cm}$, respectively. Due to its lower residual resistivity, most of the data presented here are from sample 2, though some data from sample 1 are included to demonstrate reproducibility. For both, the Hall voltage V_H at field B is taken as $\frac{1}{2}[V_{13}(B) - V_{13}(-B)]$ or $\frac{1}{2}[V_{24}(B) - V_{24}(-B)]$, where $V_{ij} \equiv V_i - V_j$, V_i is the voltage in contact i , and contact numbering is shown in Figs. 1(c,d). This procedure cancels contributions to V_H from contact misalignment. The Hall coefficient R_H is then obtained as $R_H = V_H t / (IB)$, where I is the applied current and t the sample thickness.

Longitudinal resistivity. We look first at the temperature dependence of the longitudinal resistivity ρ_{xx} at the Lifshitz transition, testing our data against three hypothesized temperature dependences. (1) $\rho_{xx} \propto T^2 \log T$. Boltzmann transport theory applied to a Fermi liquid tuned to an electron-to-hole Lifshitz transition yields a $T^2 \log T$ form [20, 21]. To obtain this result, it is nec-

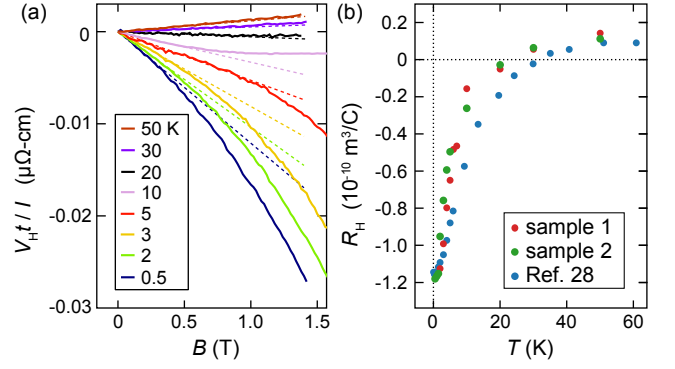


FIG. 3. (a) $V_H t / I$, where t is sample thickness and I the applied current, versus B for sample 2 at various temperatures. The dotted lines are extrapolations of linear fits over $0 < B < 0.35$ T. Equivalent data for Sample 1 are shown in [27]. (b) $R_H(T)$ of both samples at zero stress, and B up to ± 0.5 T for sample 1 and ± 0.35 T for sample 2. Data from Ref. [28] are also shown.

essary to take into account the fact that, in the absence of impurity scattering, only umklapp scattering generates resistivity. Ref. [22] finds that $\rho_{xx} \propto T^2 \log T$ also for an electron-to-open transition, as occurs here, but only if there are other bands present. (2) $\rho_{xx} \propto T^{3/2}$. The non-umklapp scattering rate, which affects *e.g.* the thermal but not the electrical resistivity, is expected to scale as $T^{3/2}$ [22]. Also, $\rho_{xx} \propto T^{3/2}$ is expected for extended saddle points [20]. (3) $\rho_{xx} \propto T^{5/3}$. This form has been observed near ferromagnetic quantum critical points [23–25]. It is understood theoretically as a result of loss of quasiparticle coherence due to the quantum criticality [24–26].

The superconductivity of Sr_2RuO_4 is strongly enhanced at the Lifshitz transition [30]. To measure ρ_{xx} at low temperatures, we suppress it with a 1.5 T field applied along the c axis. We apply a magnetoresistance model to subtract an estimate for $\Delta\rho_{xx}$, the change in ρ_{xx} under the 1.5 T field, yielding an estimate for the zero-field resistivity that would be obtained without superconductivity. For isotropic metals in weak magnetic fields,

$$\Delta\rho_{xx} \propto \omega_c^2 \tau^2 \times \rho_{xx}(B=0), \quad (1)$$

where the cyclotron frequency $\omega_c = eB/m^*$ and τ is the relaxation time. $\tau^{-1} = \alpha + \beta T^2$ is expected in the Fermi liquid regime, and in unstressed Sr_2RuO_4 it has been shown that $(\rho_{xx}/\Delta\rho_{xx})^{1/2}$ can be fitted by $\alpha + \beta T^2$ up to at least 80 K [31], even though ρ_{xx} follows a T^2 form only up to ~ 30 K [31, 32]. In Fig. 2(a) it is shown that a model $(\rho_{xx}/\Delta\rho_{xx})^{1/2} = \alpha + \beta T^2$ fits the observed magnetoresistance at each stress that we tested. We use this model to extrapolate $\Delta\rho_{xx}$ into the superconducting regime where it cannot be directly measured.

Fig. 2(b) shows $\rho_{xx}(T)$ and $\rho_{xx}(T) - \Delta\rho_{xx}(T)$ of sample 2 at $\sigma = \sigma_L$. Fig. 2(c) shows the differences between

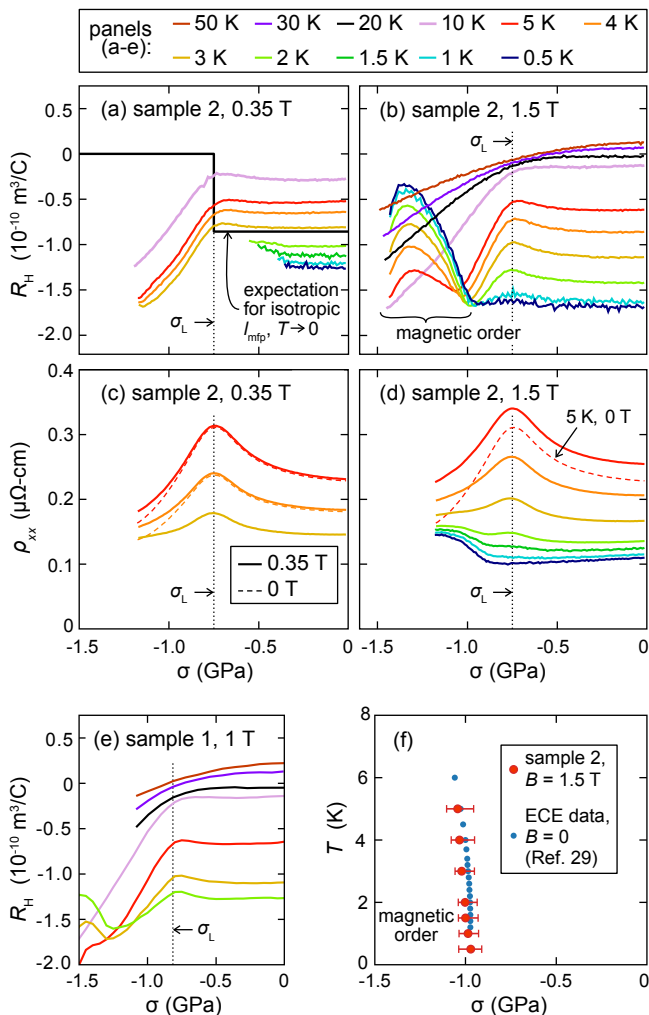


FIG. 4. (a) $R_H(\sigma)$ of sample 2 at various temperatures, measured at $B = \pm 0.35$ T. Data that are clearly affected by superconductivity are excluded. The expected $R_H(\sigma)$ for isotropic mean free path and $T \rightarrow 0$, calculated using a simple tight-binding model, is also shown. (b) $R_H(\sigma)$ of sample 2 at $B = \pm 1.5$ T, a strong enough field to fully suppress the superconductivity. (c) $\rho_{xx}(\sigma)$ of sample 2 at $B = 0$ and 0.35 T. (d) $\rho_{xx}(\sigma)$ of sample 2 at $B = 1.5$ T. (e) $R_H(\sigma)$ of sample 1 at $B = \pm 1$ T. (f) The phase boundary of the magnetic order, taken as the stresses where $d^2 R_H/dT^2$ in panel (c) is maximum. The error bars are the FWHM of the peaks in $d^2 R_H/dT^2$. Also shown is the phase boundary found in elastocaloric effect data [29], with the Lifshitz stress normalized to -0.75 GPa.

$\rho_{xx} - \Delta\rho_{xx}$ and the three hypothesised fitting models. $\rho_{xx} = \rho_0 + AT^{3/2}$ clearly does not fit the data well, while $\rho_{xx} = \rho_0 + AT^{5/3}$ and $\rho_{xx} = \rho_0 + AT^2 \log(T_0/T)$ work equally well. For the latter, we obtain $T_0 = 95$ K. In Ref. [27], we show that an alternative magnetoresistance model, $(\rho_{xx}/\Delta\rho_{xx})^{1/2} = \alpha + \beta T^{3/2}$, can also be applied at $\sigma = \sigma_L$, and does not alter the conclusion that $\rho_{xx} = \rho_0 + AT^2 \log(T_0/T)$ is a better fit to the data than $\rho_{xx} = \rho_0 + AT^{3/2}$. In contrast, in earlier work it was found that the $T^2 \log T$ and $T^{3/2}$ forms worked equally well at $\sigma =$

σ_L , over a fitting range of 4–40 K [33]. We hypothesize that this temperature range was too high to accurately capture the low-temperature behavior.

Although the $T^{5/3}$ and $T^2 \log T$ models work equally well, the hypothesis under which $T^{5/3}$ is obtained theoretically, ferromagnetic quantum criticality, appears not to apply here. NMR data on Sr_2RuO_4 show that the Stoner factor of Sr_2RuO_4 is enhanced by $\sim 30\%$ at the Lifshitz transition [34], and that there is no dramatic change in quasiparticle weight [35]. Tuning to the Lifshitz transition strengthens ferromagnetic fluctuations, but apparently not to point that they become critical.

Hall effect. We now look at the Hall effect. To investigate appropriate measurement fields, in Fig. 3(a) we show V_H versus B for sample 2. For temperatures below ~ 10 K, the low-field regime in which $V_H \propto B$ extends only up to ~ 0.3 T. Fig. 3(b) shows $R_H(T)$ of both samples in the low-field limit. R_H is hole-like at 50 K, and electron-like below ~ 20 K, as reported previously [28, 36].

Figs. 4(a,c) show $R_H(\sigma)$ and $\rho_{xx}(\sigma)$ of sample 2 at various temperatures and at ± 0.35 T, which is close to the low-field limit. Figs. 4(b,d) show the equivalent data at ± 1.5 T, which fully suppresses the superconductivity. Fig. 4(e) shows data on R_H from sample 1 at 1 T. We identify the Lifshitz stress σ_L as the peak in ρ_{xx} at 5 K, yielding $\sigma_L = -0.75 \pm 0.08$ GPa for sample 2. For sample 1, ρ_{xx} was not measured, but comparison of $R_H(\sigma)$ with that of sample 2 yields $\sigma_L = -0.82 \pm 0.08$ GPa. For temperatures of ~ 2 K and above, the data shown in Figs. 4(a, b, e) reveal that R_H decreases as samples are compressed through $\sigma = \sigma_L$, that is, moving from right to left in the graphs. Below ~ 5 K, this decrease is somewhat less steep for sample 1 than sample 2, possibly due to the stronger defect scattering, but the difference is not large. Fig. 4(a) also shows the expected $R_H(\sigma)$ for an isotropic mean free path, calculated using a tight-binding model that will be presented, and the contrast with the data is clear.

In the 1.5 T data in Figs. 4(b,d) it can be seen that below ~ 1 K, both R_H and ρ_{xx} become essentially constant across the Lifshitz transition. In other words, even in the $T \rightarrow 0$ limit, R_H does not respond as expected to the change in Fermi surface topology.

Before discussing the Hall data further, we comment briefly on stress-induced magnetic order. This order is probably an incommensurate spin density wave [37], and has a clear effect on R_H at 1.5 T. The stress range where the magnetic order condenses is indicated in Fig. 4(b). However, at 0.35 T the magnetic order has no clear effect on $R_H(\sigma)$ [see Fig. 4(a)], and at 1 T $R_H(\sigma)$ shows some response to the order but less than at 1.5 T [see Fig. 4(e)]. This variation is not because the magnetic phase boundary has strong field dependence: in Fig. 4(f), we show that the magnetic phase boundary identified in the 1.5 T data matches well that identified from elastocaloric effect

measurements in zero field [29]. Rather, there must be a strong field dependence in the effect of the magnetic phase on transport. We leave this as a topic for future investigation.

Discussion. We focus first on R_H at 5–10 K, where the downturn in R_H at $\sigma < \sigma_L$ is large and quite sharp. ρ_{xx} peaks at $\sigma = \sigma_L$ due to enhanced electron-electron scattering [21, 38], and the fact that both the downturn in R_H and the peak in ρ_{xx} fade over the same temperature range shows that the downturn in R_H is also associated with electron-electron scattering. In this section, we show that the magnitude of the change in R_H implies changes in scattering throughout the Brillouin zone, and that a model of orbital differentiation can account for the change.

Following Ref. [17], in this orbital differentiation model the band-dependent electron-electron scattering rate $\eta_\nu(\mathbf{k})$, where $\nu = \alpha, \beta, \text{ or } \gamma$, is given by:

$$\eta_\nu(\mathbf{k}) = \sum_m |\langle \chi_m(\mathbf{k}) | \psi_\nu(\mathbf{k}) \rangle|^2 \eta_m. \quad (2)$$

$\alpha, \beta,$ and γ label the Fermi surfaces— see Fig. 1(a). $|\langle \chi_m(\mathbf{k}) | \psi_\nu(\mathbf{k}) \rangle|^2$ is the weight of orbital m in band ν at momentum \mathbf{k} , and η_m is an orbital-dependent scattering rate. Scattering is taken to be a local property, so η_m has no \mathbf{k} dependence. This model is supported by photoemission and Raman scattering data [39, 40], and applies when Hund’s interactions control electronic correlations, as appears to be the case in Sr_2RuO_4 [9, 10].

We calculate the orbital weights using the simplest possible tight-binding model that reproduces the Fermi surface topology of Sr_2RuO_4 [27, 41–43]. Our model Fermi surfaces are shown in Fig. 1(b). Near-neighbour hopping integrals are taken to vary linearly with strain, with a scaling constant that is set so that the Lifshitz transition occurs at $\sigma_L = -0.75$ GPa. The Hall conductivity σ_{xy} is calculated using the Ong construction [1]:

$$\sigma_{xy} = \frac{e^3}{2\pi^2 \hbar^2} \mathbf{B} \cdot \int_{FS} \frac{d\mathbf{l}_{\text{mfp}}(\mathbf{k}) \times \mathbf{l}_{\text{mfp}}(\mathbf{k})}{2}, \quad (3)$$

where $\mathbf{l}_{\text{mfp}}(\mathbf{k})$ is the mean free path at point \mathbf{k} . Stated in words, Eq. 3 states that the Hall conductivity is determined by the curvature of the sections of Fermi surface with longer mean free path. To obtain R_H , the longitudinal conductivities σ_{xx} and σ_{yy} are needed: $R_H \approx (1/B)\sigma_{xy}/(\sigma_{xx}\sigma_{yy})$. σ_{xx} is taken to be:

$$\sigma_{xx} = \frac{e^2}{2\hbar\pi^2} \int_{FS} ds l_{\text{mfp}}(\mathbf{k}) (\mathbf{l}_{\text{mfp}} \cdot \hat{\mathbf{x}})^2. \quad (4)$$

Eq. 4 neglects the distinction between umklapp and non-umklapp processes; it is an approximate model. We also neglect impurity and phonon scattering, so $l_{\text{mfp}}(\mathbf{k}) = v_F(\mathbf{k})/\eta_\nu(\mathbf{k})$, where $v_F(\mathbf{k})$ is the Fermi velocity.

For simplicity, we assume $\eta_{xz} = \eta_{yz} = \eta_{xz,yz}$, even at nonzero stress where this equality is not symmetry-protected. R_H calculated as a function of the ratio

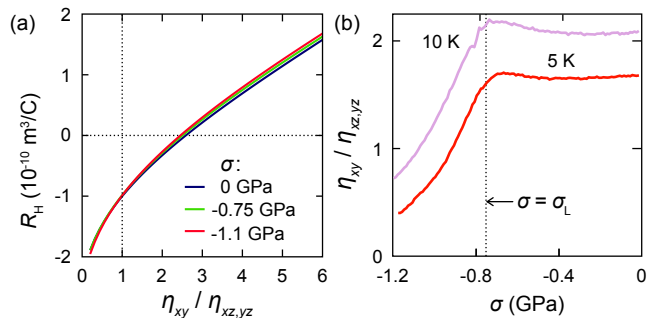


FIG. 5. (a) R_H calculated within the orbital-dependent scattering model described in the text, as a function of the ratio of xy and xz, yz scattering rates, $\eta_{xy}/\eta_{xz,yz}$. The calculation employs a simple tight-binding model of the Fermi surfaces of Sr_2RuO_4 . (b) $\eta_{xy}/\eta_{xz,yz}$ versus stress at 5 and 10 K, determined from R_H of sample 2 at ± 0.35 T and the calculation results shown in panel (a).

$\eta_{xy}/\eta_{xz,yz}$ and at three different stresses is shown in Fig. 5(a). Our results at $\sigma = 0$ match well the more accurate model of Ref. [17]. $R_H > 0$ for large $\eta_{xy}/\eta_{xz,yz}$ because both the β and γ sheets have substantial xy orbital weight. A high xy scattering rate suppresses the contribution to the Hall conductivity from these sheets, leaving that from the α sheet, which is hole-like.

We use the results shown in Fig. 5(a) to convert R_H measured at ± 0.35 T and at 5 and 10 K, temperatures where electron-electron scattering dominates [44], to $\eta_{xy}/\eta_{xz,yz}$. Results are shown in Fig. 5(b). At $\sigma = 0$, we find $\eta_{xy}/\eta_{xz,yz} > 1$. This is expected because in unstressed Sr_2RuO_4 it is the xy band that is most strongly renormalized, and the electron-electron scattering rate is correlated with the degree of renormalization [45]. Dynamical mean-field theory calculations indicate that this stronger renormalization is due to proximity to the Lifshitz transition [8, 9], which occurs in the xy band. It is therefore reasonable to hypothesize that tuning even closer to this transition would cause a further increase in $\eta_{xy}/\eta_{xz,yz}$. Such an increase is indeed visible in Fig. 5(b), but it is small. The much more prominent feature is a steep fall in $\eta_{xy}/\eta_{xz,yz}$ for $\sigma < \sigma_L$. Consistent with this interpretation that scattering in the xy band falls steeply for $\sigma < \sigma_L$, the magnetoresistance becomes much stronger for $\sigma < \sigma_L$: in Fig. 4(c), a noticeable difference appears between $\rho_{xx}(T = 5 \text{ K})$ at 0 and 0.35 T.

Even if this specific model is called into question, our data show that scattering must change throughout the Brillouin zone. Our tight-binding model yields $R_H = -1.74 \times 10^{-10} \text{ m}^3/\text{C}$ for unstressed Sr_2RuO_4 when l_{mfp} is isotropic and equal on the β and γ sheets but zero on the α sheet. The fact that R_H falls to values in this range when $\sigma < \sigma_L$ means that l_{mfp} must become long on essentially all convex portions of the β and γ sheets.

We briefly discuss the $T \rightarrow 0$ limit, where impurity scattering dominates. In this limit it is frequently as-

sumed that l_{mfp} is set by defect spacing and is therefore isotropic. However, we have already noted that with isotropic l_{mfp} R_{H} would jump upward at the Lifshitz transition, due to the change in Fermi surface topology. The fact that R_{H} remains essentially constant across $\sigma = \sigma_{\text{L}}$ indicates that l_{mfp} must be very short in the neck region of the γ sheet. The observation here that $\rho_{xx} \propto T^2 \log T$ at $\sigma = \sigma_{\text{L}}$ indicates standard quasiparticle dispersion right up to the saddle point, and we therefore hypothesize that small-angle scattering from charge disorder is stronger in these regions. Similar anisotropy is seen in overdoped cuprate superconductors, where l_{mfp} is shorter along the $(0, \pi)$ and $(\pi, 0)$ directions (the antinodal directions) [3, 4, 46], and enhanced small-angle scattering due to charge disorder is thought to play a role [3, 47].

In summary, going through the Lifshitz transition drives large changes in electron-electron scattering in Sr_2RuO_4 . In a model of orbital differentiation, the xy band transitions over a small strain range from being the most- to being the least-strongly correlated band. This result provides important information on the origin of electronic correlations in metals, and should be tested with other techniques.

APPENDIX

Sample carrier. The sample carrier used here is illustrated in Fig. S1(a). The two parts are respectively bolted to the uniaxial stress cell, which controls the distance between them. Bringing the two parts into contact compresses the sample. The set of four flexures in the sample carrier, which protect the sample from inadvertent transverse and twisting forces, are calculated to have a combined spring constant of $0.14 \text{ N}/\mu\text{m}$. This spring constant is used to calculate the force in the flexures when the sample gets compressed, and is subtracted from the force reading from the cell to obtain the force applied to the sample.

Sample 2. As described in the main text, for sample 2 a plasma focused ion beam was used to mill voltage contacts from the sample itself, ensuring highly accurate placement. In Fig. S1(b), a scanning electron micrograph of sample 2 is shown after mounting onto the sample carrier, but before the upper plates were installed. The electrical contacts at the end of the sample are visible in this SEM. In Fig. S1(c), a photograph taken after the upper plates were installed is shown. The upper plate is held in place with Stycast 2850.

The longitudinal resistivity at $\sigma = \sigma_{\text{L}}$. In the main text, we used a relationship $[\rho_{xx}(B = 0)/\Delta\rho_{xx}]^{0.5} = \alpha + \beta T^2$ to subtract the magnetoresistance and estimate the $\rho_{xx}(T)$ that would be obtained at $B = 0$ without

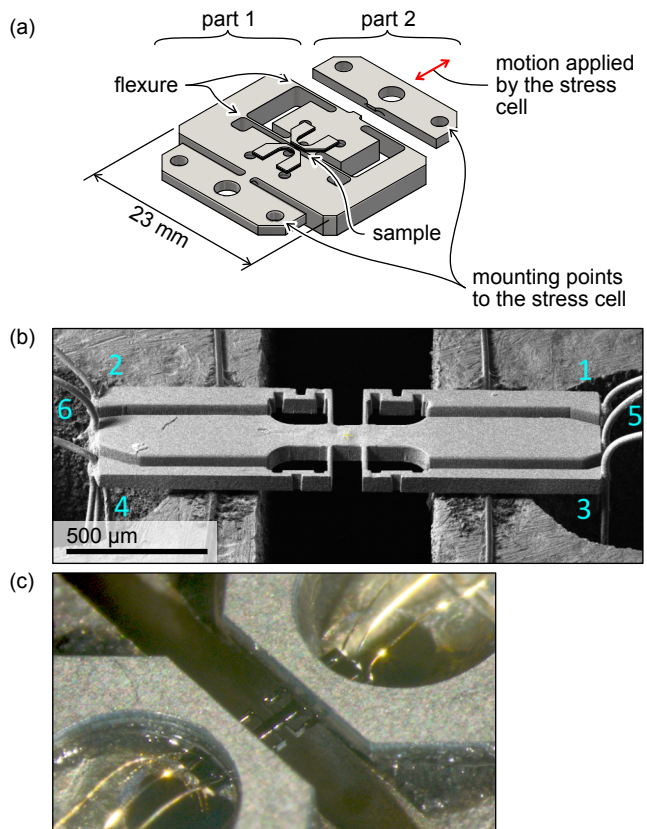


FIG. 6. (a) Illustration of the sample carrier used here. This carrier gets mounted to a uniaxial stress cell similar to that described in Ref. [18]. (b) Scanning electron micrograph of sample 2 before installation of the upper plates. (c) Photograph of sample 2 after installation of the upper plates.

superconductivity. We show in Fig. S2 that the form $[\rho_{xx}(B = 0)/\Delta\rho_{xx}]^{0.5} = \alpha + \beta T^{1.5}$ can also be fit to the data at $\sigma = \sigma_{\text{L}}$. Potentially, it is a better model because non-unklapp scattering is expected to be proportional to $T^{1.5}$ at $\sigma = \sigma_{\text{L}}$. Results when this model is used to subtract the magnetoresistivity are also shown in Fig. S2. The conclusion is the same as with the T^2 magnetoresistance model shown in the main text: $\rho_{xx} = \rho_0 + AT^{3/2}$ is a poor fit to the data, while $\rho_0 + AT^2 \log(T_0/T)$ and $\rho_0 + AT^{5/3}$ work equally well.

$V_{\text{H}}(B)$ for sample 1. In Fig. S3 we show the Hall voltage $V_{\text{H}}(B)$ for sample 1, at various temperatures. Due to its higher defect scattering, the low-field range where $V_{\text{H}} \propto B$ extends slightly further than for sample 2.

Complete data set at $B = \pm 0.35 \text{ T}$. In Fig. 4 in the main text, we excluded from panels (a) and (c), which show data at $B = \pm 0.35 \text{ T}$, data that we estimated to be affected by the superconductivity of Sr_2RuO_4 . In Fig. S4(a-b), we show the complete data set.

In Fig. S4(c) we also show an example of unsymmetrized data at 0.35 T : the voltage between contacts

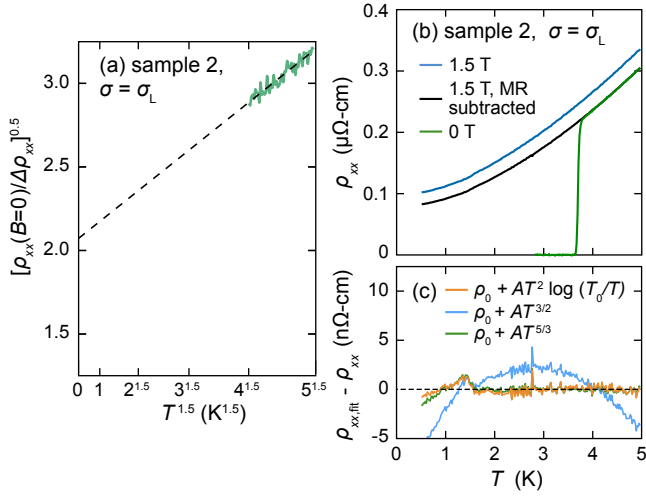


FIG. 7. An alternative magnetoresistance model. (a) $(\rho_{xx}(B=0)/\Delta\rho_{xx})^{0.5}$, where $\Delta\rho_{xx}$ is the change in ρ_{xx} between 0 and 1.5 T, against $T^{3/2}$ for sample 2 at $\sigma = \sigma_L$. (b) $\rho_{xx}(T)$ of sample 2 at $\sigma = \sigma_L$. The black line is an average of the data at +1.5 and -1.5 T with the magnetoresistance subtracted as described in the supplemental text. (c) Difference between three fitting models and the data with the magnetoresistance subtracted.

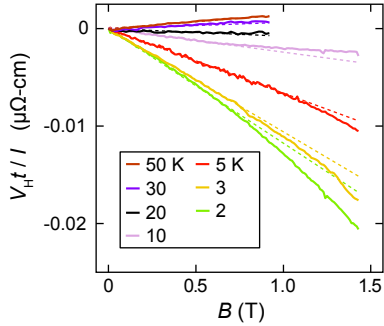


FIG. 8. Hall voltage V_H versus field B for sample 1 at various temperatures.

1 and 3 divided by the applied current. We noted in the main text that the stress-induced magnetic order has a strong effect on R_H at 1.5 T, but no discernible effect on R_H at 0.35 T. Here, it can be seen that there are anomalies in the unsymmetrized data at 0.35 T. In Fig. 4(c) in the main text, there are also no clear anomalies in $\rho_{xx}(\sigma)$ when the magnetic order onsets, so the appearance of anomalies in the unsymmetrized data suggests that the magnetic order affects ρ_{yy} and/or ρ_{zz} more strongly than R_H . ρ_{yy} and ρ_{zz} are expected to enter the unsymmetrized Hall data at some level due to misalignment of the sample axes with respect to the crystal axes; without particular effort, misalignment of $\sim 1^\circ$ is typical. The main point of showing this data is to make clear that the magnetic order is present at 0.35 T, as at 1.5 T.

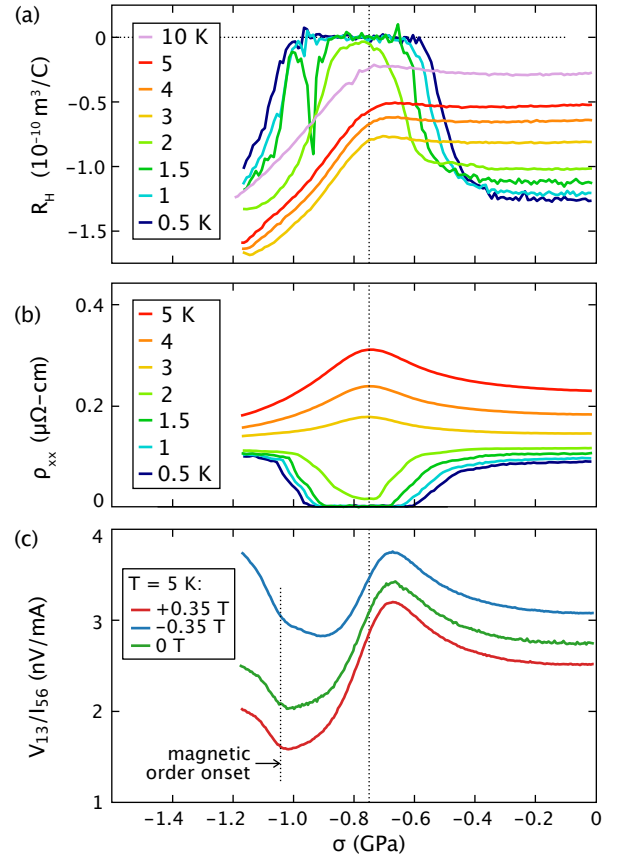


FIG. 9. (a) $R_H(\sigma)$ of sample 2, measured at $B = \pm 0.35$ T. This is a copy of Fig. 4(a) from the main text, but including the data that are affected by the superconductivity. (b) $\rho_{xx}(\sigma)$ of sample 2 at $B = +0.35$ T— Fig. 4(b) from the main text, with the data affected by the superconductivity included. (c) Unsymmetrized data at $T = 5$ K and ± 0.35 T: V_{13} , the voltage difference between contacts 1 and 3, divided by the current applied between contacts 5 and 6. The onset of the magnetic order is taken as the stress where $d^2 R_H/d\sigma^2$ at 1.5 T is maximum; see Fig. 4(d).

Tight-binding model. Our tight-binding model is:

$$H = \psi_s^\dagger(\mathbf{k}) \begin{pmatrix} E_{xz}(\mathbf{k}) & -isg & ig \\ isg & E_{yz}(\mathbf{k}) & -sg \\ -ig & -sg & E_{xy}(\mathbf{k}) \end{pmatrix} \psi_s(\mathbf{k}),$$

$$E_{xz}(\mathbf{k}) = -\mu - 2t_1 \cos k_x - 2t_2 \cos k_y,$$

$$E_{xy}(\mathbf{k}) = -\mu - 2t_3(\cos k_x + \cos k_y) - 4t_4 \cos k_x \cos k_y - 2t_5(\cos 2k_x + \cos 2k_y).$$

$\psi_s(\mathbf{k}) = [c_{\mathbf{k},xz,s}, c_{\mathbf{k},yz,s}, c_{\mathbf{k},xy,-s}]^T$, $s = \pm 1$ for spin, and $\{t_1, t_2, t_3, t_4, t_5, \mu, g\} = \{88, 9, 80, 40, 5, 109, 35\}$ meV. This model was derived as a fit to ARPES data in Ref. [41], and was also applied in in Ref. [42, 43]. These parameters yield cyclotron effective masses for the α , β , and γ sheets of 5.4, 4.8, and $16.7m_e$, respectively.

To apply uniaxial stress, x -oriented hopping integrals are scaled as $t \rightarrow t \times (1 - \alpha \varepsilon_{xx})$, and y -oriented hopping

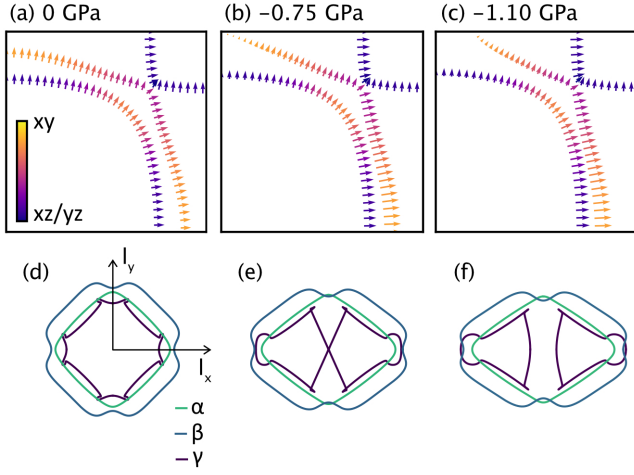


FIG. 10. (a-c) Fermi surfaces calculated using the tight-binding model described in the text. The arrow length is proportional to the Fermi velocity. (d-f) I curves under an assumption of isotropic scattering time, that is, $\eta_{xy} = \eta_{xz, yz}$. In this case, $\mathbf{l}_{\text{mfp}} \propto \mathbf{v}_F$.

integrals as $t \rightarrow t \times (1 + \alpha \nu_{xy} \varepsilon_{xx})$. ε_{xx} is the longitudinal strain, $\nu_{xy} = 0.508$ is the Poisson's ratio [48], and α is a constant that places the Lifshitz transition at $\sigma_L = -0.75$ GPa. The diagonal hopping integral, t_4 , is scaled as $t_4 \rightarrow t_4 \times [1 - \frac{\alpha}{2}(1 - \nu_{xy})\varepsilon_{xx}]$. The Fermi surfaces resulting from this tight-binding model are shown in Fig. 1 in the main text. In Figs. S5(a-c) we show these Fermi surfaces again, but populated with arrows whose lengths are proportional to the mean free path. For this illustration, we take $\eta_{xy} = \eta_{xz, yz}$, so \mathbf{l}_{mfp} is proportional to the Fermi velocity. The Ong construction is illustrated in Figs. S5(d-f). The curves shown in these panels are the paths traced when each mean free path vector \mathbf{l}_{mfp} is shifted to the origin. Ong showed that the Hall conductivity σ_{xy} is proportional to the sum of the areas enclosed.

Acknowledgements. P.Y. thanks K. Shirer and M. König for assistance with the plasma focused ion beam. We thank A. Georges, M. Zingl, and J. Mravlje for a critical read of the manuscript. We additionally thank E. Berg, N. Hussey, and J. Schmalian for useful comments. We acknowledge the financial support of the Max Planck Society. A.P.M. and C.W.H. acknowledge the financial support of the Deutsche Forschungsgemeinschaft (DFG, German Research Foundation) - TRR 288 - 422213477 (project A10). N.K. is supported by a KAKENHI Grants-in-Aids for Scientific Research (Grant Nos. 17H06136, 18K04715, and 21H01033), and Core-to-Core Program (No. JPJSCCA20170002) from the Japan Society for the Promotion of Science (JSPS) and by a JST-Mirai Program (Grant No. JPMJMI18A3). H. M. L. N. acknowledges support from the Alexander von Humboldt Foundation through a Research Fellowship for Postdoctoral Researchers. Research in Dresden benefits from the environment provided by the DFG Cluster of Excellence

ct.qmat (EXC 2147, project ID 390858940). Raw data for this publication are available at *url to be determined*.

- [1] N. P. Ong, Geometric interpretation of the weak-field hall conductivity in two-dimensional metals with arbitrary fermi surface, *Phys. Rev. B* **43**, 193 (1991).
- [2] N. Nandi, T. Scaffidi, P. Kushwaha, S. Khim, M. E. Barber, V. Sunko, F. Mazzola, P. D. C. King, H. Rosner, P. J. W. Moll, M. König, J. E. Moore, S. Hartnoll, and A. P. Mackenzie, Unconventional magneto-transport in ultrapure PdCoO₂ and PtCoO₂, *npj Quantum Mater.* **3**, 66 (2018).
- [3] A. Narduzzo, G. Albert, M. M. J. French, N. Mangkorntong, M. Nohara, H. Takagi, and N. E. Hussey, Violation of the isotropic mean free path approximation for overdoped La_{2-x}Sr_xCuO₄, *Phys. Rev. B* **77**, 220502(R) (2008).
- [4] M. M. J. French, J. G. Analytis, A. Carrington, L. Balicas, and N. E. Hussey, Tracking anisotropic scattering in overdoped Tl₂Ba₂CuO_{6+δ} above 100 K, *New J. Phys.* **11**, 055057 (2009).
- [5] Y. Maeno, H. Hashimoto, K. Yoshida, S. Nishizaki, T. Fujita, J. G. Bednorz, and F. Lichtenberg, Superconductivity in a layered perovskite without copper, *Nature* **372**, 532 (1994).
- [6] N. Kikugawa, A. P. Mackenzie, C. Bergemann, R. A. Borzi, S. A. Grigera, and Y. Maeno, Rigid-band shift of the Fermi level in the strongly correlated metal: Sr_{2-y}La_yRuO₄, *Phys. Rev. B* **70**, 060508(R) (2004).
- [7] N. Kikugawa, A. P. Mackenzie, C. Bergemann, and Y. Maeno, Low-temperature Hall effect in substituted Sr₂RuO₄, *Phys. Rev. B* **70**, 174501 (2004).
- [8] F. B. Kugler, M. Zingl, H. U. R. Strand, S.-S. B. Lee, J. von Delft, and A. Georges, Strongly Correlated Materials from a Numerical Renormalization Group Perspective: How the Fermi-Liquid State of Sr₂RuO₄ Emerges, *Phys. Rev. Lett.* **124**, 016401 (2020).
- [9] J. Mravlje, M. Aichhorn, T. Miyake, K. Haule, G. Kotliar, and A. Georges, Coherence-Incoherence Crossover and the Mass-Renormalization Puzzles in Sr₂RuO₄, *Phys. Rev. Lett.* **106**, 096401 (2011).
- [10] X. Deng, K. M. Stadler, K. Haule, A. Weichselbaum, J. von Delft, and G. Kotliar, Signatures of Mottness and Hundness in archetypal correlated metals, *Nat. Commun.* **10**, 2721 (2019).
- [11] C. Bergemann, S. R. Julian, A. P. Mackenzie, S. Nishizaki, and Y. Maeno, Detailed topography of the Fermi surface of Sr₂RuO₄, *Phys. Rev. Lett.* **84**, 2662 (2000).
- [12] C. Bergemann, A. P. Mackenzie, S. R. Julian, D. Forsythe, and E. Ohmichi, Quasi-two-dimensional Fermi liquid properties of the unconventional superconductor Sr₂RuO₄, *Adv. Phys.* **52**, 639 (2003).
- [13] V. Sunko, E. A. Morales, I. Marković, M. E. Barber, D. Milosavljević, F. Mazzola, D. A. Sokolov, N. Kikugawa, C. Cacho, P. Dudin, H. Rosner, C. W. Hicks, P. D. C. King, and A. P. Mackenzie, Direct observation of a uniaxial stress-driven Lifshitz transition in Sr₂RuO₄, *npj Quantum Mat.* **4**, 46 (2019).
- [14] M. E. Barber, F. Lechermann, S. V. Streltsov, S. L. Sko-

- rnyakov, S. Ghosh, B. J. Ramshaw, N. Kikugawa, D. A. Sokolov, A. P. Mackenzie, C. W. Hicks, and I. I. Mazin, Role of correlations in determining the Van Hove strain in Sr_2RuO_4 , *Phys. Rev. B* **100**, 245139 (2019).
- [15] A. V. Maharaj, I. Esterlis, Y. Zhang, B. J. Ramshaw, and S. A. Kivelson, Hall number across a van Hove singularity, *Phys. Rev. B* **96**, 045132 (2017).
- [16] E. K. Kokkinis, G. Goldstein, D. V. Efremov, and J. J. Betouras, Semiclassical transport with Berry curvature: Chambers formula and applications to systems with Fermi surface topological transitions, *Phys. Rev. B* **105**, 155123 (2022).
- [17] M. Zingl, J. Mravlje, M. Aichhorn, O. Parcollet, and A. Georges, Hall coefficient signals orbital differentiation in the Hund's metal Sr_2RuO_4 , *npj Quantum Mater.* **4**, 35 (2019).
- [18] M. A. Barber, A. Steppke, A. P. Mackenzie, and C. W. Hicks, Piezoelectric-based uniaxial pressure cell with integrated force and displacement sensors, *Rev. Sci. Instrum.* **90**, 023904 (2019).
- [19] F. Jerzembeck, H. S. Røising, A. Steppke, H. Rosner, D. A. Sokolov, N. Kikugawa, T. Scaffidi, S. H. Simon, A. P. Mackenzie, and C. W. Hicks, The superconductivity of Sr_2RuO_4 under *c*-axis uniaxial stress, *Nature Commun.* **13**, 4596 (2022).
- [20] R. Hlubina, Effect of impurities on the transport properties in the Van Hove scenario, *Phys. Rev. B* **53**, 11344 (1996).
- [21] C. H. Mousatov, E. Berg, and S. A. Hartnoll, Theory of the strange metal $\text{Sr}_3\text{Ru}_2\text{O}_7$, *Proc. Natl. Acad. Sci. U.S.A.* **117**, 2852 (2020).
- [22] V. C. Stangier, E. Berg, and J. Schmalian, Breakdown of the Wiedemann-Franz law at the Lifshitz point of strained Sr_2RuO_4 , *Phys. Rev. B* **105**, 115113 (2022).
- [23] M. Nicklas, M. Brando, G. Knebel, F. Mayr, W. Trinkl, and A. Loidl, Non-Fermi-Liquid Behavior at a Ferromagnetic Quantum Critical Point in $\text{Ni}_x\text{Pd}_{1-x}$, *Phys. Rev. Lett.* **82**, 4268 (1999).
- [24] R. P. Smith, M. Sutherland, G. G. Lonzarich, S. S. Saxena, N. Kimura, S. Takashima, M. Nohara, and H. Takagi, Marginal breakdown of the Fermi-liquid state on the border of metallic ferromagnetism, *Nature* **455**, 1220 (2008).
- [25] M. Sutherland, R. P. Smith, N. Marcano, Y. Zou, S. E. Rowley, F. M. Grosche, N. Kimura, S. M. Hayden, S. Takashima, M. Nohara, and H. Takagi, Transport and thermodynamic evidence for a marginal Fermi-liquid state in ZrZn_2 , *Phys. Rev. B* **85**, 035118 (2012).
- [26] J. Mathon, Magnetic and electrical properties of ferromagnetic alloys near the critical concentration, *Proc. R. Soc. A* **306**, 355 (1968).
- [27] Supplemental Material, available at *url to be determined*.
- [28] A. P. Mackenzie, N. E. Hussey, A. J. Diver, S. R. Julian, Y. Maeno, S. Nishizaki, and T. Fujita, Hall effect in the two-dimensional metal Sr_2RuO_4 , *Phys. Rev. B* **54**, 7425 (1996).
- [29] Y.-S. Li, M. Garst, J. Schmalian, N. Kikugawa, D. A. Sokolov, C. W. Hicks, F. Jerzembeck, M. S. Ikeda, A. W. Rost, M. Nicklas, and A. P. Mackenzie, Elastocaloric determination of the phase diagram of Sr_2RuO_4 , *Nature* **607**, 276 (2022).
- [30] A. Steppke, L. Zhaox, M. E. Barber, T. Scaffidi, F. Jerzembeck, H. Rosner, A. S. Gibbs, Y. Maeno, S. H. Simon, A. P. Mackenzie, and C. W. Hicks, Strong peak in T_c of Sr_2RuO_4 under uniaxial pressure, *Science* **355**, eaaf9398 (2017).
- [31] N. E. Hussey, A. P. Mackenzie, J. R. Cooper, Y. Maeno, S. Nishizaki, and T. Fujita, Normal-state magnetoresistance of Sr_2RuO_4 , *Phys. Rev. B* **57**, 5505 (1998).
- [32] Y. Maeno, K. Yoshida, H. Hashimoto, S. Nishizaki, S.-I. Ikeda, M. Nohara, T. Fujita, A. P. Mackenzie, N. E. Hussey, J. G. Bednorz, and F. Lichtenberg, Two-dimensional Fermi liquid behavior of the superconductor Sr_2RuO_4 , *J. Phys. Soc. Jpn.* **66**, 1405 (1997).
- [33] M. E. Barber, A. S. Gibbs, Y. Maeno, A. P. Mackenzie, and C. W. Hicks, Resistivity in the Vicinity of a van Hove Singularity: Sr_2RuO_4 under Uniaxial Pressure, *Phys. Rev. Lett.* **120**, 076602 (2018).
- [34] Y. Luo, A. Pustogow, P. Guzman, A. P. Dioguardi, S. M. Thomas, F. Ronning, N. Kikugawa, D. A. Sokolov, F. Jerzembeck, A. P. Mackenzie, C. W. Hicks, E. D. Bauer, I. I. Mazin, and S. E. Brown, Normal State ^{17}O NMR Studies of Sr_2RuO_4 under Uniaxial Stress, *Phys. Rev. X* **9**, 021044 (2019).
- [35] A. Chronister, M. Zingl, A. Pustogow, Y. Luo, D. A. Sokolov, F. Jerzembeck, N. Kikugawa, C. W. Hicks, J. Mravlje, E. D. Bauer, J. D. Thompson, A. P. Mackenzie, A. Georges, and S. E. Brown, Tuning the Fermi liquid crossover in Sr_2RuO_4 with uniaxial stress, *npj Quantum Mater.* **7**, 113 (2022).
- [36] N. Shirakawa, K. Murata, Y. Nishihara, S. Nishizaki, Y. Maeno, T. Fujita, J. G. Bednorz, F. Lichtenberg, and N. Hamada, Novel Hall-coefficient behavior in superconducting Sr_2RuO_4 , *J. Phys. Soc. Jpn.* **64**, 1072 (1995).
- [37] V. Grinenko, S. Ghosh, R. Sarkar, J.-C. Orain, A. Nikitin, M. Elender, D. Das, Z. Guguchia, F. Brückner, M. E. Barber, J. Park, N. Kikugawa, D. A. Sokolov, J. S. Bobowski, T. Miyoshi, Y. Maeno, A. P. Mackenzie, H. Luetkens, C. W. Hicks, and H.-H. Klauss, Split superconducting and time-reversal symmetry-breaking transitions in Sr_2RuO_4 under stress, *Nat. Phys.* **17**, 748 (2021).
- [38] F. Herman, J. Buhmann, M. H. Fischer, and M. Sigrist, Deviation from Fermi-liquid transport behavior in the vicinity of a Van Hove singularity, *Phys. Rev. B* **99**, 184107 (2019).
- [39] A. Tamai, M. Zingl, E. Rozbicki, E. Cappelli, S. Riccò, A. de la Torre, S. McKeown Walker, F. Y. Bruno, P. D. C. King, W. Meevasana, M. Shi, M. Radović, N. C. Plumb, A. S. Gibbs, A. P. Mackenzie, C. Berthod, H. U. R. Strand, M. Kim, A. Georges, and F. Baumberger, High-Resolution Photoemission on Sr_2RuO_4 Reveals Correlation-Enhanced Effective Spin-Orbit Coupling and Dominantly Local Self-Energies, *Phys. Rev. X* **9**, 021048 (2019).
- [40] J.-C. Philippe, B. Baptiste, C. Sow, Y. Maeno, A. Forget, D. Colson, M. Cazayous, A. Sacuto, and Y. Gallais, Orbital dichotomy of Fermi liquid properties in Sr_2RuO_4 revealed by Raman spectroscopy, *Phys. Rev. B* **103**, 235147 (2021).
- [41] V. B. Zabolotnyy, D. V. Evtushinsky, A. A. Kordyuk, T. K. Kim, E. Carleschi, B. P. Doyle, R. Fittipaldi, M. Cuoco, A. Vecchione, and S. V. Borisenko, Renormalized band structure of Sr_2RuO_4 : A quasiparticle tight-binding approach, *J. Electron Spectrosc. Relat. Phenom.* **191**, 48 (2013).
- [42] A. T. Rømer, D. D. Scherer, I. M. Eremin, P. J. Hirschfeld, and B. M. Andersen, Knight Shift and Lead-

- ing Superconducting Instability from Spin Fluctuations in Sr_2RuO_4 , *Phys. Rev. Lett.* **123**, 247001 (2019).
- [43] S. Cobo, F. Ahn, I. Eremin, and A. Akbari, Anisotropic spin fluctuations in Sr_2RuO_4 : Role of spin-orbit coupling and induced strain, *Phys. Rev. B* **94**, 224507 (2016).
- [44] X. Deng, K. Haule, and G. Kotliar, Transport properties of metallic ruthenates: a DFT + DMFT investigation, *Phys. Rev. Lett.* **116**, 256401 (2016).
- [45] X. Deng, A. Sternbach, K. Haule, D. N. Basov, and G. Kotliar, Shining light on transition-metal oxides: unveiling the hidden Fermi liquid, *Phys. Rev. Lett.* **113**, 246404 (2014).
- [46] J. Ayres, M. Berben, M. Čulo, Y.-T. Hsu, E. van Heumen, Y. Huang, J. Zaanen, T. Kondo, T. Takeuchi, J. R. Cooper, C. Putzke, S. Friedemann, A. Carrington, and N. E. Hussey, Incoherent transport across the strange-metal regime of overdoped cuprates, *Nature* **595**, 661 (2021).
- [47] E. Abrahams and C. M. Varma, What angle-resolved photoemission experiments tell about the microscopic theory for high-temperature superconductors, *Proc. Natl. Acad. Sci. U.S.A.* **97**, 5714 (2000).
- [48] S. Ghosh, A. Shekhter, F. Jerzembeck, N. Kikugawa, D. A. Sokolov, M. Brando, A. P. Mackenzie, C. W. Hicks, and B. J. Ramshaw, Thermodynamic evidence for a two-component superconducting order parameter in Sr_2RuO_4 , *Nat. Phys.* **17**, 199 (2021).